Thermal Convection Heated both Volumetrically and from Below: Implications for Predictions of Planetary Evolution

Gael Choblet, Edgar Marc Parmentier

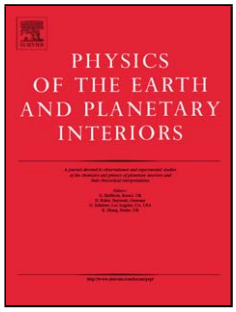

Title: Thermal Convection Heated both Volumetrically and from Below: Implications for Predictions of Planetary Evolution

Authors: G. Choblet, E.M. Parmentier

PII: S0031-9201(09)00008-9
DOI: doi:10.1016/j.pepi.2009.01.005
Reference: PEPI 5124

To appear in: *Physics of the Earth and Planetary Interiors*

Received date: 7-7-2008
Revised date: 11-11-2008
Accepted date: 14-1-2009

Please cite this article as: Choblet, G., Parmentier, E.M., Thermal Convection Heated both Volumetrically and from Below: Implications for Predictions of Planetary Evolution, *Physics of the Earth and Planetary Interiors* (2008), doi:10.1016/j.pepi.2009.01.005

Thermal Convection Heated both Volumetrically and from Below: Implications for Predictions of Planetary Evolution

G. Choblet *

Université de Nantes, Nantes Atlantique Universités, CNRS, Laboratoire de Planétologie et Géodynamique, UMR 6112, France

E. M. Parmentier

Brown University, Providence, Rhode-Island, USA

Abstract

Solid-state thermal convection, as a model for the internal dynamics of planetary mantles, is generated both by volumetric heating and heating from below. A series of 2D and 3D numerical experiments is described where a bottom heat flux is prescribed as well as a constant fraction of volumetric heating with either free-slip or no-slip conditions for the two horizontal boundaries. The assumption that hot plumes rising in the interior of the layer act as a volumetric heat source leads to a first order scaling of thermal boundary layers. Cases with a no-slip boundary agree well with this scaling while cases with free-slip systematically deviate: a decrease of 20-30 % is observed for the temperature difference across the boundary layer when the fraction of heating from below is increased from 0 to 1. These differences are attributable to a velocity structure near the boundary varying with the fraction of volumetric heating. The main planetary implications are that (i) the average ther-

mal structure of the bulk mantle and lithosphere are not good indicators of the distribution of heat sources between the interior (e.g. radioactive heating, secular cooling) and the lower interface (e.g. core cooling) ; (ii) in contrast, the nature of volcanism (wether it is localized, hot-spot like or widespread) reflect this distribution and should thus help to constrain the global thermal structure as well as the existence of a magnetic dynamo.

Key words: Planetary interiors, Mantle convection, Thermal evolution, Boundary condition

1 Introduction

Solid-state thermal convection in planetary mantles is generated both by volumetric heating and heating from below. Volumetric heating may be due to radioactive decay and tidal dissipation; and, in a steady-state approximation, secular cooling can also be approximated as a volumetric heat source (e.g. Krishnamurti, 1968a,b; Daly, 1980; Choblet and Sotin, 2000). Numerous models of thermal evolution have also assumed that heating from below can be represented as a volumetric heat source. Recent examples include thermal evolution models of Nimmo and Stevenson (2000) and Parmentier and Zuber (2007). The results of this work identify the conditions under which this is a reasonable approximation.

For terrestrial planets, cooling and solidification of the iron-rich core is a primary source of heating from below, and heat flux out of the core, transported by thermal convection in a largely solid silicate mantle, should control the

* 2, rue de la Houssinière, BP 92 208, 44 322 Nantes Cedex 3, France
Email address: Gael.Choblet@univ-nantes.fr (G. Choblet).

strength of the magnetic field along with the solidification rate of the core (e.g. Labrosse et al., 2001; Stevenson, 2001). Among the terrestrial planets, differing size of the core should imply significant differences in the relative amounts of volumetric heating and heating from below. This heating should also vary during the evolution of the planet, an effect which could be particularly large for a planet such as Mercury with a relatively large core (cf. Zuber et al., 2007). For differentiated icy satellites, radiogenic heat in a silicate core can heat an overlying icy mantle from below and tidal dissipation may heat it volumetrically. The resulting temperature distributions in the convecting icy layer will determine whether and how much of this layer will be liquid (e.g. Tobie et al., 2003; Roberts and Nimmo, 2008). For both terrestrial planets and icy satellites, the relative proportions of heating from below and volumetric heating results in variations of mantle temperature distributions that should be reflected in the style of volcanism, from one dominated by local hot spots at the top of rising plumes to more globally distributed extrusions perhaps controlled by lithospheric structure.

This study examines scaling relationships for the rate of heat transfer and thermal structure of a layer of viscous fluid heated both from within and from below. Such scaling relationships provide estimates of heat transfer rate and thermal structure leading to a first order understanding and can guide large scale models for mantle convection that, requiring specific choices for a number of physical parameter, can be carried out for a limited range of conditions. Although many previous studies have treated either volumetric heating or heating from below, few have considered their combined effects (McKenzie et al., 1974; Ishiwatari et al., 1994; Sotin and Labrosse, 1999; Shahnas et al.,

2008; Moore, 2008). Among these, only threee studies have treated systematically convection in a fluid layer with mixed heating in order to derive scaling relationships: Sotin and Labrosse (1999) derived a boundary layer analysis from 3D numerical experiments in a Cartesian framework (tested with results in a 3D spherical shell by Shahnas et al., 2008, who also address the influence of the shell thickness) and, more recently, Moore (2008) proposes a specific scaling for the bottom hot boundary layer.

This study, along with these earlier ones, consider a uniform viscosity fluid even though deformation due to thermally-activated creep is expected to be strongly temperature dependent. Studies of thermal convection in a fluid with strongly temperature-dependent viscosity both for heating from below (Solomatov, 1995) and volumetric heating (Grasset and Parmentier, 1998) along with laboratory studies for secular cooling (Davaille and Jaupart, 1993), show that convection beneath a suitably defined conductive lid near the cold top boundary may be treated as convection in an isoviscous fluid. We have considered the four combinations resulting from two possible mechanical boundary conditions (free-slip and no-slip) for the two horizontal interfaces of the fluid layer. In the case of planetary interiors, a free-slip condition may best represent the interface of a convective solid layer with an adjacent liquid layer such as a liquid iron rich-core beneath a silicate mantle in the case of most terrestrial planets but also when a deep ocean lies under or over an icy layer as is suggested for example in the case of large satellites such as Europa (e.g. Tobie et al., 2003) or Enceladus (e.g. Roberts and Nimmo, 2008); a no-slip condition (though it is not investigated as thoroughly as the free-slip boundary by previous studies) is likely to be more characteristic of the interface between two solid layers (e.g. icy layer over a silicate rich core within the satellites already mentioned). Finally, as indicated above, the stagnant lid regime is

well described by the juxtaposition of a conductive lid above an almost isoviscous convective sublayer : for this reason, in the constant viscosity framework, small-scale convection beneath the lithosphere on a one-plate terrestrial planet (beneath continents in the case of the Earth) is addressed in a better way with a no-slip condition.

Both Sotin and Labrosse (1999) and Moore (2008) treated a prescribed, uniform temperature on the bottom boundary. In constrast, we consider a prescribed heat flux since this allows a simpler approach to developing an intuitive understanding of the scaling involved. While a uniform temperature is more appropriate for the top of a very low viscosity convecting core, a prescribed heat flux might be more relevant for the interface between a deep silicate core/layer with an icy shell. We show that both uniform temperature and uniform heat flux give similar results.

2 Theoretical formulation

Equations for convection in very viscous fluids have been reported in numerous earlier studies. Adopting the Boussinesq approximation, the incompressibility condition along with the conservation equations for heat and momentum are considered. Relevant physical properties of the fluid are thermal conductivity k, thermal diffusivity κ, and viscosity μ. The fluid density with a reference value ρ_0 is treated as a linear function of temperature as described by coefficient of thermal expansion α. The nondimensionalizations use the following characteristic scales: the length scale L is chosen as the depth of the fluid layer, and the diffusive scale L^2/κ for time. The temperature scale fL/k is based on the heat-flux f through the top boundary. Note that since both the

bottom heat flux f_b and the volumetric heating rate H are prescribed, f is also a prescribed parameter in the present numerical experiments while the global temperature difference is a result of the calculations. Two dimensionless parameters are thus introduced, the Rayleigh ($\mathrm{Ra}_f = \alpha\rho_0 g f L^4/k\kappa\mu$) and Prandtl ($\mathrm{Pr} = \mu/\rho_0\kappa$) numbers. For convection in a very viscous fluid, we consider the limit of infinite Pr.

The resulting dimensionless equations are solved numerically in a rectangular two or three dimensional domain with periodic conditions on the vertical boundaries. A uniform heat flux is prescribed on the bottom, and a constant temperature on the top. Combinations of free-slip and no-slip conditions on the top and bottom boundaries considered are listed in Table 1. The aspect ratio of the domain is (1:2) in 2D and (1:1:1) in 3D.

Numerical experiments are based on solutions of the equations obtained using second order finite volume approximations for the pressure, velocity, and temperature fields on a staggered mesh. With buoyancy forces derived from the temperature field at a given time, the flow equations are solved iteratively using a multi-grid method with Gauss-Seidel smoothing in V-cycles. The advection of temperature in the energy equation is treated using an explicit scheme that minimizes numerical diffusion (Smolarkiewicz, 1984).

For the parameter ranges considered here, persistently time-dependent temperature and velocity fields are obtained. Each numerical experiment is run to a secular steady state in which the mean temperature and heat flux do not change with time, and then for a sufficiently long time interval that accurate stationary time averages can be obtained.

3 Results

A simple approximation for mixed heating would be to assume that hot plumes from the bottom thermal boundary rise into the cooler interior of the convecting fluid, losing their heat, and thus acting as a volumetric heat source. The heat flux transported through the top boundary would then follow the same scaling as for volumetric heating alone, when only a cool top boundary layer is present. Conservation of energy requires that the heat flux across the top boundary $f = f_b + HL$ (with H the dimensionless rate of volumetric heating). With scaling laws for volumetrically heated convection (Parmentier and Sotin, 2000), the dimensionless temperature difference across the top boundary is given by

$$\Delta\theta_t \propto \frac{fL}{\mathrm{kRa}_f^{1/4}} \tag{1}$$

Within the present hypothesis, the temperature difference is independent of the fraction of the heat flux derived from below ($q^* = f_b/f$). If velocities near the top and bottom boundary layers are essentially equal, then the two boundary layer thicknesses would be the same and the temperature difference across the bottom boundary layer is

$$\Delta\theta_b = q^* \Delta\theta_t \tag{2}$$

Comparison with this simple first order hypothesis then provides a basis for describing and interpreting the results of numerical experiments. Deviations from this scaling would indicate the conditions under which velocities and temperatures near the boundaries are affected by the distribution of heating. For example, it is reasonable to expect that hot plumes rising from the lower

boundary have an increasing effect on heat transfer across the top boundary layer as the fraction of heating from below increases.

The temperature differences across the top and bottom boundary layers as a function of q^* are shown in Figure 1 (a normalized temperature difference is computed using $\Delta\theta_t(q^*) = 0$ as a reference temperature difference). Time-averaged values of horizontally-averaged temperatures as a function of depth shown in Figure 2 (also displaying maximum and minimum profiles) are used to evaluate $\Delta\theta_t$ and $\Delta\theta_b$. In Figure 1-a,b,c,d, the numerical experiments correspond to a single value of $\mathrm{Ra}_f (= 10^8)$ and the temperature differences plotted are normalized by the value obtained for the volumetrically heated case ($q^* = 0$). According to the simple first order hypothesis, temperature differences across the hot and cold boundary layers would follow the solid lines shown. For the case of no-slip top (Figure 1-a) and bottom boundaries, calculated temperature differences follow this first order hypothesis very well.

As shown in Figure 1-b, the case with free-slip boundaries deviates from the simple scaling hypothesis, showing a gradual decrease of the temperature difference across both boundary layers as the amount of heating from below increases relative to the simple prediction. The temperature difference across the cold boundary layer is 30 % smaller with pure heating from below ($q^* = 1$) than with pure volumetric heating ($q^* = 0$). The hot boundary layer follows a similar trend. The slight differences between $\Delta\theta_t$ and $\Delta\theta_b$ for $q^* = 1$ are attributable to the asymmetry in the temperature boundary condition in our experiments: temperature is prescribed at the top while flux is prescribed at the bottom.

Interestingly, for cases with mixed boundary conditions (Figure 1-c,d), the variation of the temperature differences ($\Delta\theta$) with q^* reflect directly the local boundary condition on velocity or stress. For a no-slip top and a free-slip bottom (Figure 1-c), as for no-slip at both boundaries, $\Delta\theta_t$ does not vary much with q^* so that the first-order scaling is valid. The variation of $\Delta\theta_b$ with q^* is comparable to that observed for the pure free-slip case, with the exception of the value for $q^* = 1$ that is not as small. The results of Figure 1 also indicate that rising hot plumes affect the free-slip top boundary layer more strongly for a no-slip (Figure 1-d) than for a free-slip (Figure 1-b) bottom boundary. This is consistent with the observation that more widely spaced hot plumes are obtained for the no-slip bottom boundary. Larger plumes rise more rapidly, remaining hotter as they rise, and therefore more strongly perturbing the velocity and temperature fields near the top boundary.

Figure 1 also shows the variations of the maximum temperature difference across the top boundary ($\Delta\theta_t^{max}$). For the cases with a no-slip top boundary, $\Delta\theta_t^{max}$ increases with q^*. In contrast, for a free-slip top boundary, $\Delta\theta_t^{max}$ is relatively independent of q^*. For a given q^*, the difference between $\Delta\theta_t^{max}$ and $\Delta\theta_t$ indicates how much hotter localized areas at the top of hot rising plumes would be. This difference increases with q^* for all cases, but most strongly for the free-slip top boundary.

Figure 1-e,f summarizes all the numerical experiments carried out in this study (for various values of Ra_f and both 2D and 3D cases). The variation with Ra_f is accounted for in the normalization of the $\Delta\theta$ values, but the results (see Figure 3) follow the scaling (1) where the exponent is very close to $-1/4$. The same features described earlier are observed for all these cases. Cases with no-slip top follow the simple scaling of Eqs. 1 and 2. Free-slip cases, although

they exhibit more scatter, also follow the same behavior observed in Figure 1-b. Note however, that the effect of decreasing $\Delta\theta_t$ with increasing q^* seems to be enhanced in 3D calculations. Results from earlier studies (Sotin and Labrosse, 1999; Moore, 2008) lead to the same variation $\Delta\theta(q^*)$, with slightly more scatter but no consistent deviation. The need to normalize $\Delta\theta$ with a global scaling (1) may introduce some of this scatter. The general agreement indicates that the nature of the boundary condition on the bottom, whether prescribed heat flux or temperature, does not affect this behavior much.

The thickness of the cold thermal boundary layer varies with position and time but is largely controlled by the thickness that develops at stagnation points: only minor thickening occurs away from stagnation points. Thus considering the thermal structure near stagnation points allows an analysis of the main difference between free-slip and no-slip cases in terms of the structure of the velocity fields near the boundaries. In the free-slip case, the vertical velocity W associated with a hot upwelling impinging on the cold boundary layer varies linearly with depth z ($W = -Az$) while in the no-slip case, ($W = -Az^2$). With the stagnation-point thickness (δ^{sp}) defined as the depth where this vertical velocity is balanced by a diffusive velocity ($2\kappa/\delta^{sp}$), the variations of δ^{sp} can simply be expressed as a function of the appropriate vertical derivative ($D^nW = d^nW/dz^n$) in dimensionless variables:

$$\delta^{sp} = \left(\frac{2}{D^nW}\right)^{1/(n+1)} \tag{3}$$

with $n = 1$ for free-slip and $n = 2$ for no-slip. δ^{sp} and D^nW for cases presented in Figure 1-a,b, are plotted in Figure 4, and show that the scaling (3) correctly describes the variations of stagnation point thicknesses with q^*. For the free-slip case δ^{sp} and D^nW vary significantly with q^* and in such a way that (3)

is satisfied. In contrast, the results for the no-slip boundary do not vary much with q^* and, with the smaller variation, a clear trend with increasing q^* cannot be discerned.

We conclude here that the decrease of the temperature difference across the cold boundary layer as the fraction of heating from below increases can be attributed mostly to the velocity structure near the boundary. For the free-slip boundary the vertical velocity is affected by the distribution of heating, particularly the strength of the hot plumes rising from the lower boundary, much more than for the no-slip boundary. This results in an increase of W with increasing q^* and thus a decrease of the stagnation point thickness mainly responsible for the decrease of the average temperature differences $\Delta\theta_t$ and $\Delta\theta_b$ relative to the simple scaling.

4 Conclusions

A simple scaling in which heat from the lower boundary can be treated as an additional volumetric heat source provides a first order description for the case of a no-slip top boundary. For a free-slip top boundary, however, both the top boundary layer temperature difference and thickness decrease relative to the prediction of this simple scaling by about 20-30 % with increasing q^*. For the same heat flux, whether a uniform temperature or a uniform heat flux condition is prescribed on the lower boundary does not appear to influence the temperature difference across the top boundary layer.

A compilation of earlier results with a prescribed uniform basal temperature (Sotin and Labrosse, 1999; Moore, 2008) together with results from this study

with a prescribed basal heat flux indicates that the trends observed in all the experiments for the temperature difference across boundary layers as a function of the amount of basal heating are similar (Fig. 1-f).

Our results show that hot plumes rising from lower boundary have a much stronger influence on velocity and thermal structure of the top boundary layer for a free-slip top boundary. For a no-slip top boundary, the simple scaling implies that the effect of hot plumes on the boundary layer structure is remarkably small. As shown in Figure 1, the effect of rising hot plumes on the free-slip top boundary layer is larger for a no-slip (Fig. 1-b) than for a free-slip (Fig. 1-d) bottom boundary. This is consistent with the observation that more widely spaced hot plumes are larger for the free-slip bottom boundary. Larger plumes remain hotter and rise more rapidly therefore more strongly perturbing the velocity and temperature fields near the top boundary. The mechanical boundary conditions thus have an important influence on the thermal structure of boundary layers.

As indicated earlier, in the case of planetary interiors, a free-slip condition may best represent the (liquid) core-(solid) mantle boundary from the mantle "point of view". A no-slip condition may be more characteristic of the interface between a cold and viscous plate and a convective mantle. For a planet in which the lithosphere acts as a conductive lid, the scaling for no-slip boundaries thus indicate that the thermal evolution of the mantle and the average thermal structure of the planetary lithosphere should not strongly reflect the distribution of heating, whether by cooling of the core, radiogenic heating or secular cooling.

In contrast, the difference between the maximum and the average tempera-

ture beneath the top boundary layer increases with q^* (see Fig. 1 and Fig.2). Since the maximum temperature at a given depth depends significantly on the distribution of heating, the nature of volcanism should remain an important indication of the distribution of heating. For example, a transition from globally distributed volcanic activity, reflecting widespread partial melting beneath the thermal boundary layer, to localized hot spot volcanism should indicate the changing relative importance of secular cooling (volumetric heating) and heat flux out of the core. Note that the heterogeneous distribution of radioactive elements, especially if heat-producing elements are concentrated in a deep region, as is suggested in models advocating a deep-enriched reservoir for the Earth (e.g. Tackley, 2000) or, as a possible result of the overturn of a magma ocean cumulate on Mars (e.g. Elkins-Tanton et al., 2005), can also shape this distribution of heat. The distribution of volcanism should thus help to constrain the global thermal structure as well as the existence of a magnetic dynamo. Conversely, the average thermal structure of the lithosphere should be a good indicator of the global heat flux, but the distribution of volcanism should not since this depends significantly on the distribution of heating

Acknowledgments

We thank Stéphane Labrosse for the suggestions in his review. This work benefited from the ETHER project of the french Agence Nationale de la Recherche (ANR). The participation of EMP was supported by a grant from the NASA Geology and Geophysics Program.

References

Choblet, G., Sotin, C., 2000. 3D thermal convection with variable viscosity: can transient cooling be described by a steady state scaling law ? Phys. Earth Planet. Inter. 119, 321–336.

Daly, S., 1980. Convection with decaying heat sources: constant viscosity. Geophys. J. R. Astron. Soc. 61, 519–547.

Davaille, A., Jaupart, C., 1993. Transient high-rayleigh-number thermal convection with large viscosity variations. J. Fluid Mech. 253, 141–166.

Elkins-Tanton, L. T., Zaranek, S. E., Parmentier, E. M., Hess, P. C., 2005. Early magnetic field and magmatic activity on Mars from magma ocean cumulate overturn. Earth Planet. Sci. Lett. 236, 1–12.

Grasset, O., Parmentier, E. M., 1998. Thermal convection in a volumetrically heated, infinite Prandtl number fluid with strongly temperature-dependent viscosity: Implications for planetary evolution. J. Geophys. Res. 103, 18171–18181.

Ishiwatari, M., Takehiro, S.-I., Hayashi, Y.-Y., 1994. The effects of thermal conditions on the cell sizes of two-dimensional convection. J. Fluid Mech. 281, 33–50.

Krishnamurti, R., 1968a. Finite amplitude convection with changing mean temperature. part 1. theory. J. Fluid Mech. 33, 445–455.

Krishnamurti, R., 1968b. Finite amplitude convection with changing mean temperature. part2. an experimental test of the theory. J. Fluid Mech. 33, 457–463.

Labrosse, S., Poirier, J.-P., Le Mouël, J.-L., 2001. The age of the inner core. Earth Planet. Sci. Lett. 190, 111–123.

McKenzie, D. P., Roberts, J. M., Weiss, N. O., 1974. Convection in the earth's

mantle, towards a numerical simulation. J. Fluid Mech. 62, 465–538.

Moore, W. B., 2008. Heat transport in a convecting layer heated from within and below. J. Geophys. Res. submitted.

Nimmo, F., Stevenson, D. J., 2000. Influence of early plate tectonics on the thermal evolution and magnetic field of Mars. J. Geophys. Res. 105, 11969–11980.

Parmentier, E. M., Sotin, C., 2000. Three-dimensional numerical experiments on thermal convection in a very viscous fluid: Implications for the dynamics of a thermal boundary layer at high Rayleigh number. Phys. Fluids 12, 609–617.

Parmentier, E. M., Zuber, M. T., 2007. Early evolution of Mars with mantle compositional stratification or hydrothermal crustal cooling. J. Geophys. Res. 112, 2007–+.

Roberts, J. H., Nimmo, F., 2008. Tidal heating and the long-term stability of a subsurface ocean on Enceladus. Icarus 194, 675–689.

Shahnas, M. H., Lowman, J. P., Jarvis, G. T., Bunge, H.-P., 2008. Convection in a spherical shell heated by an isothermal core and internal sources: Implications for the thermal state of planetary mantles. Phys. Earth Planet. Inter. 168, 6–15.

Smolarkiewicz, P., 1984. A fully multidimensional positive definite advection transport algorithm with small implicit diffusion. J. Comput. Phys. 54, 325–362.

Solomatov, V. S., 1995. Scaling of temperature- and stress-dependent viscosity convection. Phys. Fluids 7, 266–274.

Sotin, C., Labrosse, S., 1999. Three-dimensional thermal convection in an isoviscous, infinite Prandtl number fluid heated from within and from below: applications to the transfer of heat through planetary mantles. Phys. Earth

337 Planet. Inter. 112, 171–190.

338 Stevenson, D. J., 2001. Mars' core and magnetism. Nature 412, 214–219.

339 Tackley, P. J., 2000. Mantle convection and plate tectonics: toward an inte-
340 grated physical and chemical theory. Science 288, 2002–2007.

341 Tobie, G., Choblet, G., Sotin, C., 2003. Tidally heated convection: constraints
342 on europa's ice shell thickness. J. Geophys. Res. 108, 5124.

343 Zuber, M. T., Aharonson, O., Aurnou, J. M., Cheng, A. F., Hauck, S. A.,
344 Heimpel, M. H., Neumann, G. A., Peale, S. J., Phillips, R. J., Smith, D. E.,
345 Solomon, S. C., Stanley, S., 2007. The Geophysics of Mercury: Current
346 Status and Anticipated Insights from the MESSENGER Mission. Space
347 Sci. Rev. 131, 105–132.

Table 1: List of the (2D and 3D) numerical experiments conducted for the present study. BC denotes the mechanical condition for the top and bottom boundaries (FS: free-slip, NS: no-slip). W_{up} and W_{do} refer to the maximum upwelling and downwelling velocities.

2D-3D	BC_{top}	BC_{bot}	Ra_f	q^*	$\Delta\theta_t$	$\Delta\theta_b$	W_{up}	W_{do}
2D	NS	NS	1.00E+08	-0.2	3.717E-02	—	6.861E+02	1.539E+03
2D	NS	NS	1.00E+08	0	3.796E-02	—	7.992E+02	1.697E+03
2D	NS	NS	1.00E+08	0.2	3.877E-02	9.501E-03	1.049E+03	1.862E+03
2D	NS	NS	1.00E+08	0.4	3.884E-02	1.659E-02	1.290E+03	2.003E+03
2D	NS	NS	1.00E+08	0.5	3.885E-02	2.009E-02	1.442E+03	2.078E+03
2D	NS	NS	1.00E+08	0.6	3.850E-02	2.268E-02	1.465E+03	1.969E+03
2D	NS	NS	1.00E+08	0.7	3.835E-02	2.679E-02	1.711E+03	2.186E+03
2D	NS	NS	1.00E+08	0.8	3.839E-02	3.026E-02	1.950E+03	2.325E+03
2D	NS	NS	1.00E+08	0.9	3.829E-02	3.370E-02	2.189E+03	2.442E+03
2D	NS	NS	1.00E+08	1	3.778E-02	3.673E-02	2.212E+03	2.361E+03
2D	NS	NS	1.00E+07	0	6.373E-02	—	2.775E+02	5.431E+02
2D	NS	NS	1.00E+07	0.2	6.683E-02	1.491E-02	3.382E+02	6.511E+02

2D	NS	NS	1.00E+07	0.4	6.576E-02	2.623E-02	4.125E+02	6.408E+02
2D	NS	NS	1.00E+07	0.6	6.485E-02	3.757E-02	5.106E+02	7.225E+02
2D	NS	NS	1.00E+06	0	1.174E-01	—	9.016E+01	2.339E+02
2D	NS	NS	1.00E+06	0.1	1.179E-01	1.390E-02	1.103E+02	2.531E+02
2D	NS	NS	1.00E+06	0.2	1.183E-01	2.313E-02	1.309E+02	2.716E+02
2D	FS	FS	1.00E+08	-0.2	2.383E-02	—	6.484E+02	1.875E+03
2D	FS	FS	1.00E+08	0	2.379E-02	—	7.427E+02	2.084E+03
2D	FS	FS	1.00E+08	0.2	2.344E-02	4.581E-03	9.982E+02	2.319E+03
2D	FS	FS	1.00E+08	0.4	2.284E-02	8.344E-03	1.351E+03	2.517E+03
2D	FS	FS	1.00E+08	0.5	2.243E-02	9.958E-03	1.310E+03	2.430E+03
2D	FS	FS	1.00E+08	0.6	2.207E-02	1.169E-02	1.728E+03	2.752E+03
2D	FS	FS	1.00E+08	0.7	2.148E-02	1.321E-02	1.938E+03	2.799E+03
2D	FS	FS	1.00E+08	0.8	2.090E-02	1.475E-02	2.258E+03	3.084E+03
2D	FS	FS	1.00E+08	0.9	2.030E-02	1.590E-02	2.745E+03	3.569E+03
2D	FS	FS	1.00E+08	1	1.694E-02	1.467E-02	3.615E+03	3.443E+03
2D	FS	FS	1.00E+08	0	2.364E-02	—	7.157E+02	1.994E+03
2D	FS	FS	1.00E+08	0.2	2.334E-02	4.459E-03	8.332E+02	2.148E+03

2D	FS	FS	1.00E+08	0.4	2.288E-02	8.416E-03	1.172E+03	2.462E+03
2D	FS	FS	1.00E+08	0.6	2.182E-02	1.162E-02	1.465E+03	2.523E+03
2D	FS	FS	1.00E+08	0.8	2.074E-02	1.471E-02	1.949E+03	2.879E+03
2D	FS	FS	1.00E+08	1	1.849E-02	1.535E-02	3.084E+03	3.770E+03
2D	NS	FS	1.00E+08	0	3.812E-02	—	7.957E+02	1.773E+03
2D	NS	FS	1.00E+08	0.2	3.879E-02	4.707E-03	1.078E+03	1.942E+03
2D	NS	FS	1.00E+08	0.4	3.878E-02	8.492E-03	1.449E+03	2.117E+03
2D	NS	FS	1.00E+08	0.5	3.880E-02	1.027E-02	1.613E+03	2.176E+03
2D	NS	FS	1.00E+08	0.6	3.842E-02	1.209E-02	1.928E+03	2.295E+03
2D	NS	FS	1.00E+08	0.7	3.829E-02	1.383E-02	2.240E+03	2.408E+03
2D	NS	FS	1.00E+08	0.8	3.822E-02	1.552E-02	2.550E+03	2.489E+03
2D	NS	FS	1.00E+08	0.9	3.807E-02	1.721E-02	3.289E+03	2.555E+03
2D	NS	FS	1.00E+08	1	3.721E-02	1.874E-02	3.748E+03	2.120E+03
2D	FS	NS	1.00E+08	0	2.378E-02	—	7.463E+02	2.099E+03
2D	FS	NS	1.00E+08	0.2	2.355E-02	9.678E-03	9.647E+02	2.272E+03
2D	FS	NS	1.00E+08	0.4	2.314E-02	1.709E-02	1.249E+03	2.486E+03
2D	FS	NS	1.00E+08	0.5	2.267E-02	2.053E-02	1.404E+03	2.531E+03

2D	FS	NS	1.00E+08	0.6	2.213E-02	2.386E-02	1.555E+03	2.613E+03
2D	FS	NS	1.00E+08	0.7	2.178E-02	2.726E-02	1.739E+03	2.755E+03
2D	FS	NS	1.00E+08	0.8	2.155E-02	3.053E-02	1.911E+03	2.992E+03
2D	FS	NS	1.00E+08	0.9	2.159E-02	3.352E-02	1.992E+03	3.402E+03
2D	FS	NS	1.00E+08	1	2.145E-02	3.644E-02	2.079E+03	3.795E+03
3D	FS	FS	1.00E+08	0	2.418E-02	—	5.760E+02	3.027E+03
3D	FS	FS	1.00E+08	0.1	2.418E-02	1.752E-03	6.287E+02	3.307E+03
3D	FS	FS	1.00E+08	0.2	2.423E-02	3.642E-03	7.747E+02	3.458E+03
3D	FS	FS	1.00E+08	0.3	2.408E-02	5.440E-03	1.016E+03	3.638E+03
3D	FS	FS	1.00E+08	0.4	2.368E-02	7.320E-03	1.306E+03	3.653E+03
3D	FS	FS	1.00E+08	0.6	2.211E-02	1.064E-02	1.822E+03	3.635E+03
3D	FS	FS	1.00E+08	0.8	2.078E-02	1.262E-02	2.789E+03	4.864E+03
3D	FS	FS	1.00E+08	1	1.676E-02	1.507E-02	4.354E+03	4.522E+03
3D	NS	NS	1.00E+08	0	3.380E-02	—	6.415E+02	1.956E+03
3D	NS	NS	1.00E+08	0	6.116E-02	—	2.060E+02	7.562E+02
3D	NS	NS	1.00E+08	0.1	3.366E-02	3.881E-03	7.528E+02	2.034E+03
3D	NS	NS	1.00E+08	0.2	3.346E-02	7.093E-03	9.412E+02	2.072E+03

3D	NS	NS	1.00E+08	0.3	3.325E-02	9.934E-03	1.123E+03	2.146E+03
3D	NS	NS	1.00E+08	0.4	3.277E-02	1.263E-02	1.385E+03	2.249E+03
3D	NS	NS	1.00E+08	0.6	3.278E-02	1.799E-02	1.987E+03	2.690E+03
3D	NS	NS	1.00E+08	0.8	3.293E-02	2.468E-02	2.758E+03	3.546E+03
3D	NS	NS	1.00E+08	0.9	3.254E-02	2.722E-02	3.095E+03	3.878E+03
3D	NS	NS	1.00E+07	1	3.204E-02	2.965E-02	3.650E+03	3.624E+03

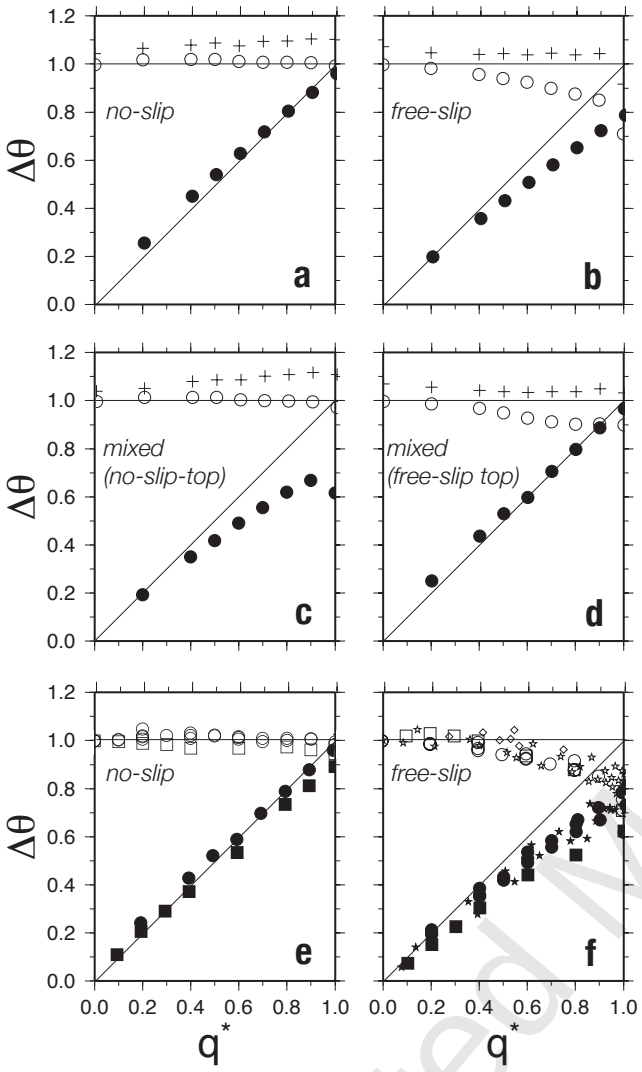

Fig. 1. Normalized temperature difference ($\Delta\tilde{\theta}$) across the boundary layers as a function of fraction of heating from below (q^*) for various mechanical boundary conditions. All panels report dimensionless values for $\Delta\theta_b$ (filled symbols), $\Delta\theta_t$ (empty symbols) and $\Delta\theta_t^{max}$ (crosses) normalized by $\Delta\theta_t(q^* = 0)$ (free-slip or no-slip, all heating from within). The horizontal and diagonal lines refer to the simple hypothetical scaling discussed in the text. Upper panels (a,b,c,d): 2D numerical experiments with $\mathrm{Ra}_f = 10^8$. Purely no-slip (a) or free-slip (b) and cases with (mixed) conditions: no-slip top and free-slip bottom (c) or the reverse (d). Lower panels (e,f): all numerical experiments performed for this study (2D: circles, 3D, squares) as well as results from previous studies shown by stars (Moore, 2008) and diamonds (Sotin and Labrosse, 1999).

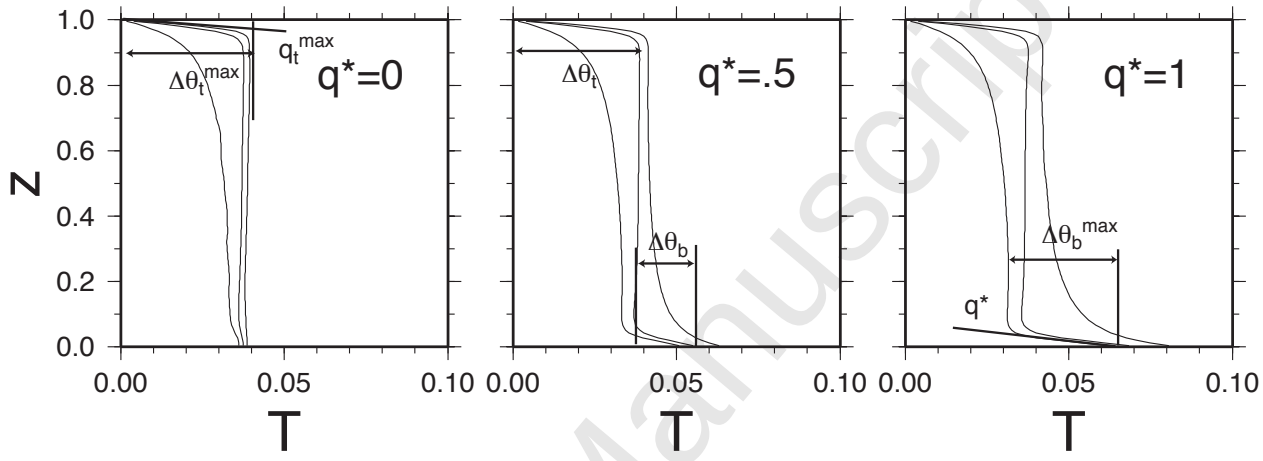

Fig. 2. Time-averaged temperatures as a function of depth. On each panel, three profiles are displayed: horizontally-averaged , minimum and maximum temperatures at a given depth. Three values of the fraction of basal heating (q^*) are shown for free-slip boundaries and $\mathrm{Ra}_f = 10^8$. Bold lines and arrows describe the procedure chosen to evaluate the temperature differences ($\Delta\theta_t, \Delta\theta_b$) and the maximum (minimum) temperature differences ($\Delta\theta_t^{max}, \Delta\theta_b^{max}$) from the various profiles. Note that since heat-flux is prescribed on the bottom boundary, all profiles have the same slope there while the slopes differ at the the top boundary ($q_t^{max} > 1$).

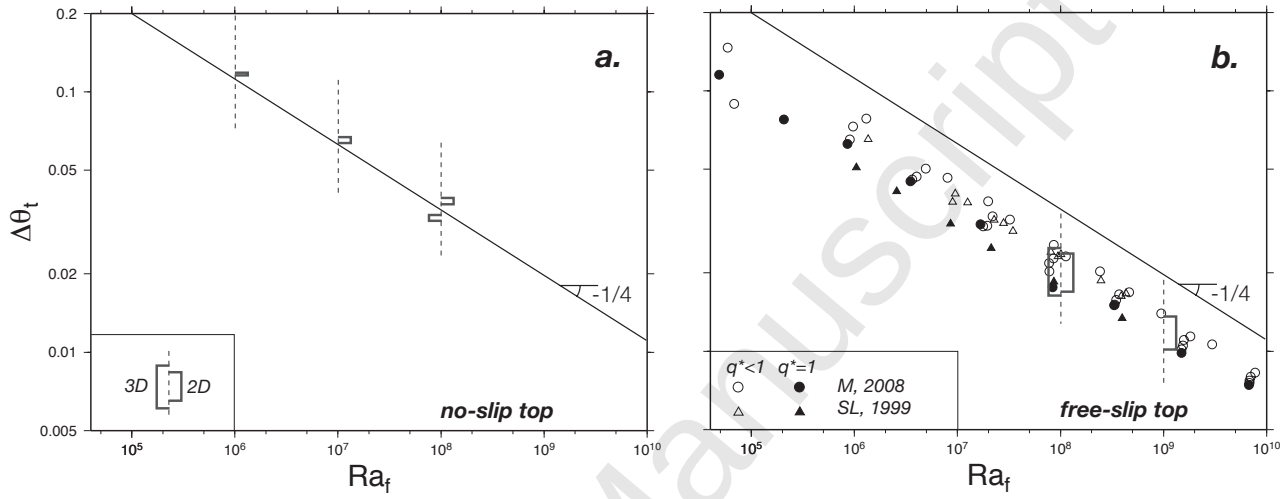

Fig. 3. Temperature difference across top thermal boundary layer ($\Delta\theta_t$) as a function of the flux-based Rayleigh number (Ra_f). The straight line shows an ideal $\mathrm{Ra}_f^{-1/4}$ scaling as in Eq. 1. (a) Results from numerical experiments with a no-slip top boundary. For each of the three values of Ra_f, the ranges including all the result is displayed as a rectangle with a missing side (on the right for 3D, on the left for 2D). (b) Results from numerical experiments with a free-slip top boundary. As in (a) results from this study are displayed using rectangles. Results from previous studies are shown by circles (Moore, 2008) and triangles (Sotin and Labrosse, 1999). Empty symbols refer to mixed heating while filled symbols refer to only heating from below.

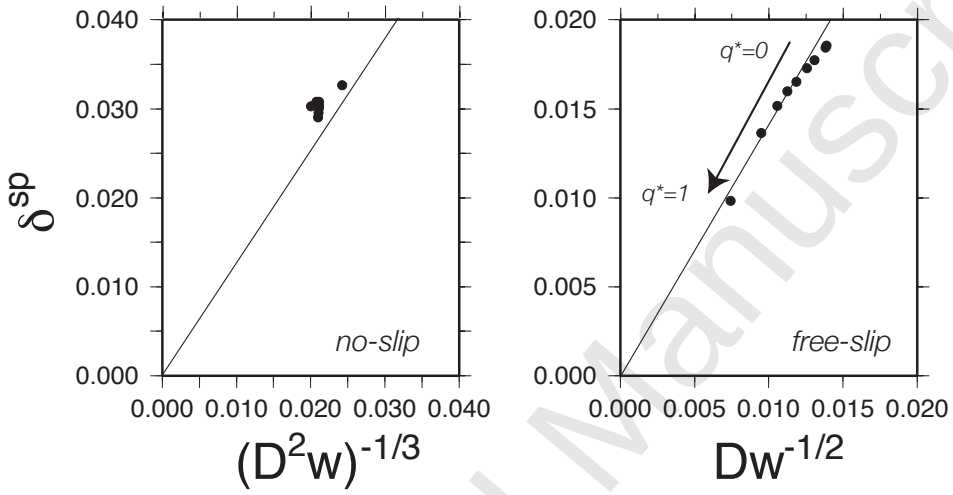

Fig. 4. Stagnation-point boundary layer thickness $\delta^{sp}(= \Delta\theta_t^{max}/q_t^{max})$ as a function of the appropriate vertical velocity derivative $D^n W$ (computed from the maximum vertical velocity profile at each time-step, averaged through time). Purely no-slip and purely free-slip results also shown in Figure 1-a,b ($\mathrm{Ra}_f = 10^8$). Lines refer to the simple stagnation-point scaling indicated in the text (3).

Thermal Convection Heated both Volumetrically and from Below: Implications for Predictions of Planetary Evolution

G. Choblet *

Université de Nantes, Nantes Atlantique Universités, CNRS, Laboratoire de Planétologie et Géodynamique, UMR 6112, France

E. M. Parmentier

Brown University, Providence, Rhode-Island, USA

Abstract

Solid-state thermal convection, as a model for the internal dynamics of planetary mantles, is generated both by volumetric heating and heating from below. A series of 2D and 3D numerical experiments is described where a bottom heat flux is prescribed as well as a constant fraction of volumetric heating with either free-slip or no-slip conditions for the two horizontal boundaries. The assumption that hot plumes rising in the interior of the layer act as a volumetric heat source leads to a first order scaling of thermal boundary layers. Cases with a no-slip boundary agree well with this scaling while cases with free-slip systematically deviate: a decrease of 20-30 % is observed for the temperature difference across the boundary layer when the fraction of heating from below is increased from 0 to 1. These differences are attributable to a velocity structure near the boundary varying with the fraction of volumetric heating. The main planetary implications are that (i) the average ther-

mal structure of the bulk mantle and lithosphere are not good indicators of the distribution of heat sources between the interior (e.g. radioactive heating, secular cooling) and the lower interface (e.g. core cooling) ; (ii) in contrast, the nature of volcanism (wether it is localized, hot-spot like or widespread) reflect this distribution and should thus help to constrain the global thermal structure as well as the existence of a magnetic dynamo.

Key words: Planetary interiors, Mantle convection, Thermal evolution, Boundary condition

1 Introduction

Solid-state thermal convection in planetary mantles is generated both by volumetric heating and heating from below. Volumetric heating may be due to radioactive decay and tidal dissipation; and, in a steady-state approximation, secular cooling can also be approximated as a volumetric heat source (e.g. Krishnamurti, 1968a,b; Daly, 1980; Choblet and Sotin, 2000). Numerous models of thermal evolution have also assumed that heating from below can be represented as a volumetric heat source. Recent examples include thermal evolution models of Nimmo and Stevenson (2000) and Parmentier and Zuber (2007). The results of this work identify the conditions under which this is a reasonable approximation.

For terrestrial planets, cooling and solidification of the iron-rich core is a primary source of heating from below, and heat flux out of the core, transported by thermal convection in a largely solid silicate mantle, should control the

* 2, rue de la Houssinière, BP 92 208, 44 322 Nantes Cedex 3, France
Email address: Gael.Choblet@univ-nantes.fr (G. Choblet).

strength of the magnetic field along with the solidification rate of the core (e.g. Labrosse et al., 2001; Stevenson, 2001). Among the terrestrial planets, differing size of the core should imply significant differences in the relative amounts of volumetric heating and heating from below. This heating should also vary during the evolution of the planet, an effect which could be particularly large for a planet such as Mercury with a relatively large core (cf. Zuber et al., 2007). For differentiated icy satellites, radiogenic heat in a silicate core can heat an overlying icy mantle from below and tidal dissipation may heat it volumetrically. The resulting temperature distributions in the convecting icy layer will determine whether and how much of this layer will be liquid (e.g. Tobie et al., 2003; Roberts and Nimmo, 2008). For both terrestrial planets and icy satellites, the relative proportions of heating from below and volumetric heating results in variations of mantle temperature distributions that should be reflected in the style of volcanism, from one dominated by local hot spots at the top of rising plumes to more globally distributed extrusions perhaps controlled by lithospheric structure.

This study examines scaling relationships for the rate of heat transfer and thermal structure of a layer of viscous fluid heated both from within and from below. Such scaling relationships provide estimates of heat transfer rate and thermal structure leading to a first order understanding and can guide large scale models for mantle convection that, requiring specific choices for a number of physical parameter, can be carried out for a limited range of conditions. Although many previous studies have treated either volumetric heating or heating from below, few have considered their combined effects (McKenzie et al., 1974; Ishiwatari et al., 1994; Sotin and Labrosse, 1999; Shahnas et al.,

2008; Moore, 2008). Among these, only threee studies have treated systematically convection in a fluid layer with mixed heating in order to derive scaling relationships: Sotin and Labrosse (1999) derived a boundary layer analysis from 3D numerical experiments in a Cartesian framework (tested with results in a 3D spherical shell by Shahnas et al., 2008, who also address the influence of the shell thickness) and, more recently, Moore (2008) proposes a specific scaling for the bottom hot boundary layer.

This study, along with these earlier ones, consider a uniform viscosity fluid even though deformation due to thermally-activated creep is expected to be strongly temperature dependent. Studies of thermal convection in a fluid with strongly temperature-dependent viscosity both for heating from below (Solomatov, 1995) and volumetric heating (Grasset and Parmentier, 1998) along with laboratory studies for secular cooling (Davaille and Jaupart, 1993), show that convection beneath a suitably defined conductive lid near the cold top boundary may be treated as convection in an isoviscous fluid. We have considered the four combinations resulting from two possible mechanical boundary conditions (free-slip and no-slip) for the two horizontal interfaces of the fluid layer. In the case of planetary interiors, a free-slip condition may best represent the interface of a convective solid layer with an adjacent liquid layer such as a liquid iron rich-core beneath a silicate mantle in the case of most terrestrial planets but also when a deep ocean lies under or over an icy layer as is suggested for example in the case of large satellites such as Europa (e.g. Tobie et al., 2003) or Enceladus (e.g. Roberts and Nimmo, 2008); a no-slip condition (though it is not investigated as thoroughly as the free-slip boundary by previous studies) is likely to be more characteristic of the interface between two solid layers (e.g. icy layer over a silicate rich core within the satellites already mentioned). Finally, as indicated above, the stagnant lid regime is

well described by the juxtaposition of a conductive lid above an almost isoviscous convective sublayer : for this reason, in the constant viscosity framework, small-scale convection beneath the lithosphere on a one-plate terrestrial planet (beneath continents in the case of the Earth) is addressed in a better way with a no-slip condition.

Both Sotin and Labrosse (1999) and Moore (2008) treated a prescribed, uniform temperature on the bottom boundary. In constrast, we consider a prescribed heat flux since this allows a simpler approach to developing an intuitive understanding of the scaling involved. While a uniform temperature is more appropriate for the top of a very low viscosity convecting core, a prescribed heat flux might be more relevant for the interface between a deep silicate core/layer with an icy shell. We show that both uniform temperature and uniform heat flux give similar results.

2 Theoretical formulation

Equations for convection in very viscous fluids have been reported in numerous earlier studies. Adopting the Boussinesq approximation, the incompressibility condition along with the conservation equations for heat and momentum are considered. Relevant physical properties of the fluid are thermal conductivity k, thermal diffusivity κ, and viscosity μ. The fluid density with a reference value ρ_0 is treated as a linear function of temperature as described by coefficient of thermal expansion α. The nondimensionalizations use the following characteristic scales: the length scale L is chosen as the depth of the fluid layer, and the diffusive scale L^2/κ for time. The temperature scale fL/k is based on the heat-flux f through the top boundary. Note that since both the

bottom heat flux f_b and the volumetric heating rate H are prescribed, f is also a prescribed parameter in the present numerical experiments while the global temperature difference is a result of the calculations. Two dimensionless parameters are thus introduced, the Rayleigh ($\mathrm{Ra}_f = \alpha\rho_0 g f L^4/k\kappa\mu$) and Prandtl ($\mathrm{Pr} = \mu/\rho_0\kappa$) numbers. For convection in a very viscous fluid, we consider the limit of infinite Pr.

The resulting dimensionless equations are solved numerically in a rectangular two or three dimensional domain with periodic conditions on the vertical boundaries. A uniform heat flux is prescribed on the bottom, and a constant temperature on the top. Combinations of free-slip and no-slip conditions on the top and bottom boundaries considered are listed in Table 1. The aspect ratio of the domain is (1:2) in 2D and (1:1:1) in 3D.

Numerical experiments are based on solutions of the equations obtained using second order finite volume approximations for the pressure, velocity, and temperature fields on a staggered mesh. With buoyancy forces derived from the temperature field at a given time, the flow equations are solved iteratively using a multi-grid method with Gauss-Seidel smoothing in V-cycles. The advection of temperature in the energy equation is treated using an explicit scheme that minimizes numerical diffusion (Smolarkiewicz, 1984).

For the parameter ranges considered here, persistently time-dependent temperature and velocity fields are obtained. Each numerical experiment is run to a secular steady state in which the mean temperature and heat flux do not change with time, and then for a sufficiently long time interval that accurate stationary time averages can be obtained.

3 Results

A simple approximation for mixed heating would be to assume that hot plumes from the bottom thermal boundary rise into the cooler interior of the convecting fluid, losing their heat, and thus acting as a volumetric heat source. The heat flux transported through the top boundary would then follow the same scaling as for volumetric heating alone, when only a cool top boundary layer is present. Conservation of energy requires that the heat flux across the top boundary $f = f_b + HL$ (with H the dimensionless rate of volumetric heating). With scaling laws for volumetrically heated convection (Parmentier and Sotin, 2000), the dimensionless temperature difference across the top boundary is given by

$$\Delta\theta_t \propto \frac{fL}{\mathrm{kRa}_f^{1/4}} \tag{1}$$

Within the present hypothesis, the temperature difference is independent of the fraction of the heat flux derived from below ($q^* = f_b/f$). If velocities near the top and bottom boundary layers are essentially equal, then the two boundary layer thicknesses would be the same and the temperature difference across the bottom boundary layer is

$$\Delta\theta_b = q^* \Delta\theta_t \tag{2}$$

Comparison with this simple first order hypothesis then provides a basis for describing and interpreting the results of numerical experiments. Deviations from this scaling would indicate the conditions under which velocities and temperatures near the boundaries are affected by the distribution of heating. For example, it is reasonable to expect that hot plumes rising from the lower

boundary have an increasing effect on heat transfer across the top boundary layer as the fraction of heating from below increases.

The temperature differences across the top and bottom boundary layers as a function of q^* are shown in Figure 1 (a normalized temperature difference is computed using $\Delta\theta_t(q^*) = 0$ as a reference temperature difference). Time-averaged values of horizontally-averaged temperatures as a function of depth shown in Figure 2 (also displaying maximum and minimum profiles) are used to evaluate $\Delta\theta_t$ and $\Delta\theta_b$. In Figure 1-a,b,c,d, the numerical experiments correspond to a single value of $\mathrm{Ra}_f (= 10^8)$ and the temperature differences plotted are normalized by the value obtained for the volumetrically heated case ($q^* = 0$). According to the simple first order hypothesis, temperature differences across the hot and cold boundary layers would follow the solid lines shown. For the case of no-slip top (Figure 1-a) and bottom boundaries, calculated temperature differences follow this first order hypothesis very well.

As shown in Figure 1-b, the case with free-slip boundaries deviates from the simple scaling hypothesis, showing a gradual decrease of the temperature difference across both boundary layers as the amount of heating from below increases relative to the simple prediction. The temperature difference across the cold boundary layer is 30 % smaller with pure heating from below ($q^* = 1$) than with pure volumetric heating ($q^* = 0$). The hot boundary layer follows a similar trend. The slight differences between $\Delta\theta_t$ and $\Delta\theta_b$ for $q^* = 1$ are attributable to the asymmetry in the temperature boundary condition in our experiments: temperature is prescribed at the top while flux is prescribed at the bottom.

Interestingly, for cases with mixed boundary conditions (Figure 1-c,d), the variation of the temperature differences ($\Delta\theta$) with q^* reflect directly the local boundary condition on velocity or stress. For a no-slip top and a free-slip bottom (Figure 1-c), as for no-slip at both boundaries, $\Delta\theta_t$ does not vary much with q^* so that the first-order scaling is valid. The variation of $\Delta\theta_b$ with q^* is comparable to that observed for the pure free-slip case, with the exception of the value for $q^* = 1$ that is not as small. The results of Figure 1 also indicate that rising hot plumes affect the free-slip top boundary layer more strongly for a no-slip (Figure 1-d) than for a free-slip (Figure 1-b) bottom boundary. This is consistent with the observation that more widely spaced hot plumes are obtained for the no-slip bottom boundary. Larger plumes rise more rapidly, remaining hotter as they rise, and therefore more strongly perturbing the velocity and temperature fields near the top boundary.

Figure 1 also shows the variations of the maximum temperature difference across the top boundary ($\Delta\theta_t^{max}$). For the cases with a no-slip top boundary, $\Delta\theta_t^{max}$ increases with q^*. In contrast, for a free-slip top boundary, $\Delta\theta_t^{max}$ is relatively independent of q^*. For a given q^*, the difference between $\Delta\theta_t^{max}$ and $\Delta\theta_t$ indicates how much hotter localized areas at the top of hot rising plumes would be. This difference increases with q^* for all cases, but most strongly for the free-slip top boundary.

Figure 1-e,f summarizes all the numerical experiments carried out in this study (for various values of Ra_f and both 2D and 3D cases). The variation with Ra_f is accounted for in the normalization of the $\Delta\theta$ values, but the results (see Figure 3) follow the scaling (1) where the exponent is very close to $-1/4$. The same features described earlier are observed for all these cases. Cases with no-slip top follow the simple scaling of Eqs. 1 and 2. Free-slip cases, although

they exhibit more scatter, also follow the same behavior observed in Figure 1-b. Note however, that the effect of decreasing $\Delta\theta_t$ with increasing q^* seems to be enhanced in 3D calculations. Results from earlier studies (Sotin and Labrosse, 1999; Moore, 2008) lead to the same variation $\Delta\theta(q^*)$, with slightly more scatter but no consistent deviation. The need to normalize $\Delta\theta$ with a global scaling (1) may introduce some of this scatter. The general agreement indicates that the nature of the boundary condition on the bottom, whether prescribed heat flux or temperature, does not affect this behavior much.

The thickness of the cold thermal boundary layer varies with position and time but is largely controlled by the thickness that develops at stagnation points: only minor thickening occurs away from stagnation points. Thus considering the thermal structure near stagnation points allows an analysis of the main difference between free-slip and no-slip cases in terms of the structure of the velocity fields near the boundaries. In the free-slip case, the vertical velocity W associated with a hot upwelling impinging on the cold boundary layer varies linearly with depth z ($W = -Az$) while in the no-slip case, ($W = -Az^2$). With the stagnation-point thickness (δ^{sp}) defined as the depth where this vertical velocity is balanced by a diffusive velocity ($2\kappa/\delta^{sp}$), the variations of δ^{sp} can simply be expressed as a function of the appropriate vertical derivative ($D^nW = d^nW/dz^n$) in dimensionless variables:

$$\delta^{sp} = \left(\frac{2}{D^nW}\right)^{1/(n+1)} \tag{3}$$

with $n = 1$ for free-slip and $n = 2$ for no-slip. δ^{sp} and D^nW for cases presented in Figure 1-a,b, are plotted in Figure 4, and show that the scaling (3) correctly describes the variations of stagnation point thicknesses with q^*. For the free-slip case δ^{sp} and D^nW vary significantly with q^* and in such a way that (3)

is satisfied. In contrast, the results for the no-slip boundary do not vary much with q^* and, with the smaller variation, a clear trend with increasing q^* cannot be discerned.

We conclude here that the decrease of the temperature difference across the cold boundary layer as the fraction of heating from below increases can be attributed mostly to the velocity structure near the boundary. For the free-slip boundary the vertical velocity is affected by the distribution of heating, particularly the strength of the hot plumes rising from the lower boundary, much more than for the no-slip boundary. This results in an increase of W with increasing q^* and thus a decrease of the stagnation point thickness mainly responsible for the decrease of the average temperature differences $\Delta\theta_t$ and $\Delta\theta_b$ relative to the simple scaling.

4 Conclusions

A simple scaling in which heat from the lower boundary can be treated as an additional volumetric heat source provides a first order description for the case of a no-slip top boundary. For a free-slip top boundary, however, both the top boundary layer temperature difference and thickness decrease relative to the prediction of this simple scaling by about 20-30 % with increasing q^*. For the same heat flux, whether a uniform temperature or a uniform heat flux condition is prescribed on the lower boundary does not appear to influence the temperature difference across the top boundary layer.

A compilation of earlier results with a prescribed uniform basal temperature (Sotin and Labrosse, 1999; Moore, 2008) together with results from this study

with a prescribed basal heat flux indicates that the trends observed in all the experiments for the temperature difference across boundary layers as a function of the amount of basal heating are similar (Fig. 1-f).

Our results show that hot plumes rising from lower boundary have a much stronger influence on velocity and thermal structure of the top boundary layer for a free-slip top boundary. For a no-slip top boundary, the simple scaling implies that the effect of hot plumes on the boundary layer structure is remarkably small. As shown in Figure 1, the effect of rising hot plumes on the free-slip top boundary layer is larger for a no-slip (Fig. 1-b) than for a free-slip (Fig. 1-d) bottom boundary. This is consistent with the observation that more widely spaced hot plumes are larger for the free-slip bottom boundary. Larger plumes remain hotter and rise more rapidly therefore more strongly perturbing the velocity and temperature fields near the top boundary. The mechanical boundary conditions thus have an important influence on the thermal structure of boundary layers.

As indicated earlier, in the case of planetary interiors, a free-slip condition may best represent the (liquid) core-(solid) mantle boundary from the mantle "point of view". A no-slip condition may be more characteristic of the interface between a cold and viscous plate and a convective mantle. For a planet in which the lithosphere acts as a conductive lid, the scaling for no-slip boundaries thus indicate that the thermal evolution of the mantle and the average thermal structure of the planetary lithosphere should not strongly reflect the distribution of heating, whether by cooling of the core, radiogenic heating or secular cooling.

In contrast, the difference between the maximum and the average tempera-

ture beneath the top boundary layer increases with q^* (see Fig. 1 and Fig.2). Since the maximum temperature at a given depth depends significantly on the distribution of heating, the nature of volcanism should remain an important indication of the distribution of heating. For example, a transition from globally distributed volcanic activity, reflecting widespread partial melting beneath the thermal boundary layer, to localized hot spot volcanism should indicate the changing relative importance of secular cooling (volumetric heating) and heat flux out of the core. Note that the heterogeneous distribution of radioactive elements, especially if heat-producing elements are concentrated in a deep region, as is suggested in models advocating a deep-enriched reservoir for the Earth (e.g. Tackley, 2000) or, as a possible result of the overturn of a magma ocean cumulate on Mars (e.g. Elkins-Tanton et al., 2005), can also shape this distribution of heat. The distribution of volcanism should thus help to constrain the global thermal structure as well as the existence of a magnetic dynamo. Conversely, the average thermal structure of the lithosphere should be a good indicator of the global heat flux, but the distribution of volcanism should not since this depends significantly on the distribution of heating

References

Choblet, G., Sotin, C., 2000. 3D thermal convection with variable viscosity: can transient cooling be described by a steady state scaling law ? Phys. Earth Planet. Inter. 119, 321–336.

Daly, S., 1980. Convection with decaying heat sources: constant viscosity. Geophys. J. R. Astron. Soc. 61, 519–547.

Davaille, A., Jaupart, C., 1993. Transient high-rayleigh-number thermal convection with large viscosity variations. J. Fluid Mech. 253, 141–166.

Elkins-Tanton, L. T., Zaranek, S. E., Parmentier, E. M., Hess, P. C., 2005. Early magnetic field and magmatic activity on Mars from magma ocean cumulate overturn. Earth Planet. Sci. Lett. 236, 1–12.

Grasset, O., Parmentier, E. M., Aug. 1998. Thermal convection in a volumetrically heated, infinite Prandtl number fluid with strongly temperature-dependent viscosity: Implications for planetary evolution. J. Geophys. Res. 103, 18171–18181.

Ishiwatari, M., Takehiro, S.-I., Hayashi, Y.-Y., 1994. The effects of thermal conditions on the cell sizes of two-dimensional convection. J. Fluid Mech. 281, 33–50.

Krishnamurti, R., 1968a. Finite amplitude convection with changing mean temperature. part 1. theory. J. Fluid Mech. 33, 445–455.

Krishnamurti, R., 1968b. Finite amplitude convection with changing mean temperature. part2. an experimental test of the theory. J. Fluid Mech. 33, 457–463.

Labrosse, S., Poirier, J.-P., Le Mouël, J.-L., Aug. 2001. The age of the inner core. Earth Planet. Sci. Lett. 190, 111–123.

McKenzie, D. P., Roberts, J. M., Weiss, N. O., 1974. Convection in the earth's mantle, towards a numerical simulation. J. Fluid Mech. 62, 465–538.

Moore, W. B., 2008. Heat transport in a convecting layer heated from within and below. J. Geophys. Res. submitted.

Nimmo, F., Stevenson, D. J., May 2000. Influence of early plate tectonics on the thermal evolution and magnetic field of Mars. J. Geophys. Res. 105, 11969–11980.

Parmentier, E. M., Sotin, C., Mar. 2000. Three-dimensional numerical experiments on thermal convection in a very viscous fluid: Implications for the dynamics of a thermal boundary layer at high Rayleigh number. Phys.

Fluids 12, 609–617.

Parmentier, E. M., Zuber, M. T., Feb. 2007. Early evolution of Mars with mantle compositional stratification or hydrothermal crustal cooling. J. Geophys. Res. 112, 2007–+.

Roberts, J. H., Nimmo, F., Apr. 2008. Tidal heating and the long-term stability of a subsurface ocean on Enceladus. Icarus 194, 675–689.

Shahnas, M. H., Lowman, J. P., Jarvis, G. T., Bunge, H.-P., 2008. Convection in a spherical shell heated by an isothermal core and internal sources: Implications for the thermal state of planetary mantles. Phys. Earth Planet. Inter. 168, 6–15.

Smolarkiewicz, P., 1984. A fully multidimensional positive definite advection transport algorithm with small implicit diffusion. J. Comput. Phys. 54, 325–362.

Solomatov, V. S., 1995. Scaling of temperature- and stress-dependent viscosity convection. Phys. Fluids 7, 266–274.

Sotin, C., Labrosse, S., Apr. 1999. Three-dimensional thermal convection in an iso-viscous, infinite Prandtl number fluid heated from within and from below: applications to the transfer of heat through planetary mantles. Phys. Earth Planet. Inter. 112, 171–190.

Stevenson, D. J., Jul. 2001. Mars' core and magnetism. Nature 412, 214–219.

Tackley, P. J., 2000. Mantle convection and plate tectonics: toward an integrated physical and chemical theory. Science 288, 2002–2007.

Tobie, G., Choblet, G., Sotin, C., 2003. Tidally heated convection: constraints on europa's ice shell thickness. J. Geophys. Res. 108, 5124.

Zuber, M. T., Aharonson, O., Aurnou, J. M., Cheng, A. F., Hauck, S. A., Heimpel, M. H., Neumann, G. A., Peale, S. J., Phillips, R. J., Smith, D. E., Solomon, S. C., Stanley, S., Aug. 2007. The Geophysics of Mercury: Current

341 Status and Anticipated Insights from the MESSENGER Mission. Space Sci.
342 Rev. 131, 105–132.

Table 1: List of the (2D and 3D) numerical experiments conducted for the present study. BC denotes the mechanical condition for the top and bottom boundaries (FS: free-slip, NS: no-slip). W_{up} and W_{do} refer to the maximum upwelling and downwelling velocities.

2D-3D	BC_{top}	BC_{bot}	Ra_f	q^*	$\Delta\theta_t$	$\Delta\theta_b$	W_{up}	W_{do}
2D	NS	NS	1.00E+08	-0.2	3.717E-02	—	6.861E+02	1.539E+03
2D	NS	NS	1.00E+08	0	3.796E-02	—	7.992E+02	1.697E+03
2D	NS	NS	1.00E+08	0.2	3.877E-02	9.501E-03	1.049E+03	1.862E+03
2D	NS	NS	1.00E+08	0.4	3.884E-02	1.659E-02	1.290E+03	2.003E+03
2D	NS	NS	1.00E+08	0.5	3.885E-02	2.009E-02	1.442E+03	2.078E+03
2D	NS	NS	1.00E+08	0.6	3.850E-02	2.268E-02	1.465E+03	1.969E+03
2D	NS	NS	1.00E+08	0.7	3.835E-02	2.679E-02	1.711E+03	2.186E+03
2D	NS	NS	1.00E+08	0.8	3.839E-02	3.026E-02	1.950E+03	2.325E+03
2D	NS	NS	1.00E+08	0.9	3.829E-02	3.370E-02	2.189E+03	2.442E+03
2D	NS	NS	1.00E+08	1	3.778E-02	3.673E-02	2.212E+03	2.361E+03
2D	NS	NS	1.00E+07	0	6.373E-02	—	2.775E+02	5.431E+02
2D	NS	NS	1.00E+07	0.2	6.683E-02	1.491E-02	3.382E+02	6.511E+02

2D	NS	NS	1.00E+07	0.4	6.576E-02	2.623E-02	4.125E+02	6.408E+02
2D	NS	NS	1.00E+07	0.6	6.485E-02	3.757E-02	5.106E+02	7.225E+02
2D	NS	NS	1.00E+06	0	1.174E-01	—	9.016E+01	2.339E+02
2D	NS	NS	1.00E+06	0.1	1.179E-01	1.390E-02	1.103E+02	2.531E+02
2D	NS	NS	1.00E+06	0.2	1.183E-01	2.313E-02	1.309E+02	2.716E+02
2D	FS	FS	1.00E+08	-0.2	2.383E-02	—	6.484E+02	1.875E+03
2D	FS	FS	1.00E+08	0	2.379E-02	—	7.427E+02	2.084E+03
2D	FS	FS	1.00E+08	0.2	2.344E-02	4.581E-03	9.982E+02	2.319E+03
2D	FS	FS	1.00E+08	0.4	2.284E-02	8.344E-03	1.351E+03	2.517E+03
2D	FS	FS	1.00E+08	0.5	2.243E-02	9.958E-03	1.310E+03	2.430E+03
2D	FS	FS	1.00E+08	0.6	2.207E-02	1.169E-02	1.728E+03	2.752E+03
2D	FS	FS	1.00E+08	0.7	2.148E-02	1.321E-02	1.938E+03	2.799E+03
2D	FS	FS	1.00E+08	0.8	2.090E-02	1.475E-02	2.258E+03	3.084E+03
2D	FS	FS	1.00E+08	0.9	2.030E-02	1.590E-02	2.745E+03	3.569E+03
2D	FS	FS	1.00E+08	1	1.694E-02	1.467E-02	3.615E+03	3.443E+03
2D	FS	FS	1.00E+08	0	2.364E-02	—	7.157E+02	1.994E+03
2D	FS	FS	1.00E+08	0.2	2.334E-02	4.459E-03	8.332E+02	2.148E+03

2D	FS	FS	1.00E+08	0.4	2.288E-02	8.416E-03	1.172E+03	2.462E+03
2D	FS	FS	1.00E+08	0.6	2.182E-02	1.162E-02	1.465E+03	2.523E+03
2D	FS	FS	1.00E+08	0.8	2.074E-02	1.471E-02	1.949E+03	2.879E+03
2D	FS	FS	1.00E+08	1	1.849E-02	1.535E-02	3.084E+03	3.770E+03
2D	NS	FS	1.00E+08	0	3.812E-02	—	7.957E+02	1.773E+03
2D	NS	FS	1.00E+08	0.2	3.879E-02	4.707E-03	1.078E+03	1.942E+03
2D	NS	FS	1.00E+08	0.4	3.878E-02	8.492E-03	1.449E+03	2.117E+03
2D	NS	FS	1.00E+08	0.5	3.880E-02	1.027E-02	1.613E+03	2.176E+03
2D	NS	FS	1.00E+08	0.6	3.842E-02	1.209E-02	1.928E+03	2.295E+03
2D	NS	FS	1.00E+08	0.7	3.829E-02	1.383E-02	2.240E+03	2.408E+03
2D	NS	FS	1.00E+08	0.8	3.822E-02	1.552E-02	2.550E+03	2.489E+03
2D	NS	FS	1.00E+08	0.9	3.807E-02	1.721E-02	3.289E+03	2.555E+03
2D	NS	FS	1.00E+08	1	3.721E-02	1.874E-02	3.748E+03	2.120E+03
2D	FS	NS	1.00E+08	0	2.378E-02	—	7.463E+02	2.099E+03
2D	FS	NS	1.00E+08	0.2	2.355E-02	9.678E-03	9.647E+02	2.272E+03
2D	FS	NS	1.00E+08	0.4	2.314E-02	1.709E-02	1.249E+03	2.486E+03
2D	FS	NS	1.00E+08	0.5	2.267E-02	2.053E-02	1.404E+03	2.531E+03

2D	FS	NS	1.00E+08	0.6	2.213E-02	2.386E-02	1.555E+03	2.613E+03
2D	FS	NS	1.00E+08	0.7	2.178E-02	2.726E-02	1.739E+03	2.755E+03
2D	FS	NS	1.00E+08	0.8	2.155E-02	3.053E-02	1.911E+03	2.992E+03
2D	FS	NS	1.00E+08	0.9	2.159E-02	3.352E-02	1.992E+03	3.402E+03
2D	FS	NS	1.00E+08	1	2.145E-02	3.644E-02	2.079E+03	3.795E+03
3D	FS	FS	1.00E+08	0	2.418E-02	—	5.760E+02	3.027E+03
3D	FS	FS	1.00E+08	0.1	2.418E-02	1.752E-03	6.287E+02	3.307E+03
3D	FS	FS	1.00E+08	0.2	2.423E-02	3.642E-03	7.747E+02	3.458E+03
3D	FS	FS	1.00E+08	0.3	2.408E-02	5.440E-03	1.016E+03	3.638E+03
3D	FS	FS	1.00E+08	0.4	2.368E-02	7.320E-03	1.306E+03	3.653E+03
3D	FS	FS	1.00E+08	0.6	2.211E-02	1.064E-02	1.822E+03	3.635E+03
3D	FS	FS	1.00E+08	0.8	2.078E-02	1.262E-02	2.789E+03	4.864E+03
3D	FS	FS	1.00E+08	1	1.676E-02	1.507E-02	4.354E+03	4.522E+03
3D	NS	NS	1.00E+08	0	3.380E-02	—	6.415E+02	1.956E+03
3D	NS	NS	1.00E+08	0	6.116E-02	—	2.060E+02	7.562E+02
3D	NS	NS	1.00E+08	0.1	3.366E-02	3.881E-03	7.528E+02	2.034E+03
3D	NS	NS	1.00E+08	0.2	3.346E-02	7.093E-03	9.412E+02	2.072E+03

3D	NS	NS	1.00E+08	0.3	3.325E-02	9.934E-03	1.123E+03	2.146E+03
3D	NS	NS	1.00E+08	0.4	3.277E-02	1.263E-02	1.385E+03	2.249E+03
3D	NS	NS	1.00E+08	0.6	3.278E-02	1.799E-02	1.987E+03	2.690E+03
3D	NS	NS	1.00E+08	0.8	3.293E-02	2.468E-02	2.758E+03	3.546E+03
3D	NS	NS	1.00E+08	0.9	3.254E-02	2.722E-02	3.095E+03	3.878E+03
3D	NS	NS	1.00E+07	1	3.204E-02	2.965E-02	3.650E+03	3.624E+03

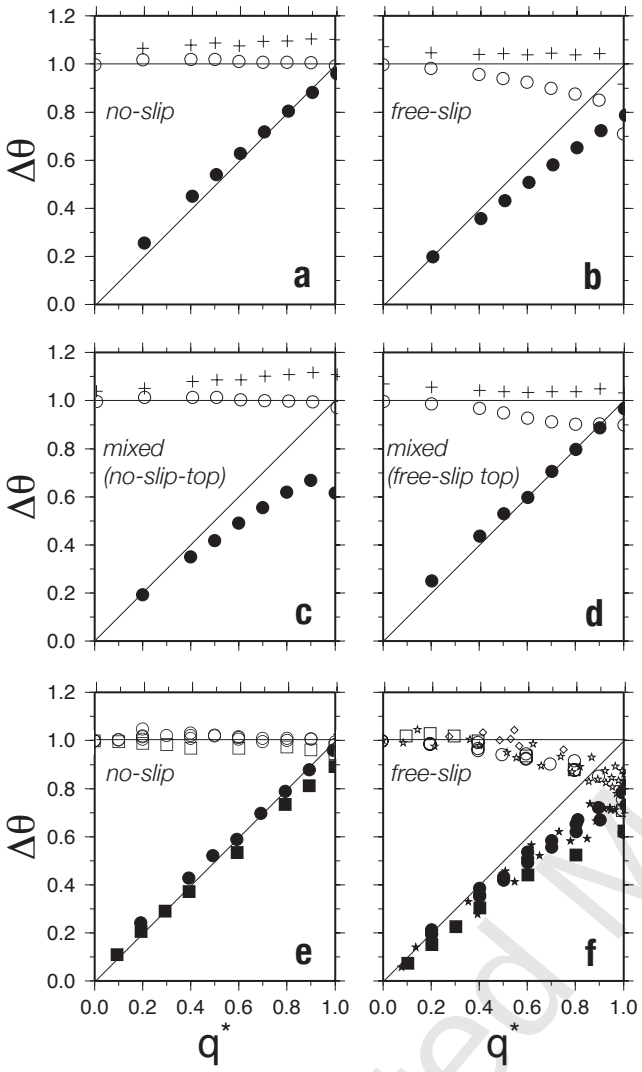

Fig. 1. Normalized temperature difference ($\Delta\tilde{\theta}$) across the boundary layers as a function of fraction of heating from below (q^*) for various mechanical boundary conditions. All panels report dimensionless values for $\Delta\theta_b$ (filled symbols), $\Delta\theta_t$ (empty symbols) and $\Delta\theta_t^{max}$ (crosses) normalized by $\Delta\theta_t(q^* = 0)$ (free-slip or no-slip, all heating from within). The horizontal and diagonal lines refer to the simple hypothetical scaling discussed in the text. Upper panels (a,b,c,d): 2D numerical experiments with $\mathrm{Ra}_f = 10^8$. Purely no-slip (a) or free-slip (b) and cases with (mixed) conditions: no-slip top and free-slip bottom (c) or the reverse (d). Lower panels (e,f): all numerical experiments performed for this study (2D: circles, 3D, squares) as well as results from previous studies shown by stars (Moore, 2008) and diamonds (Sotin and Labrosse, 1999).

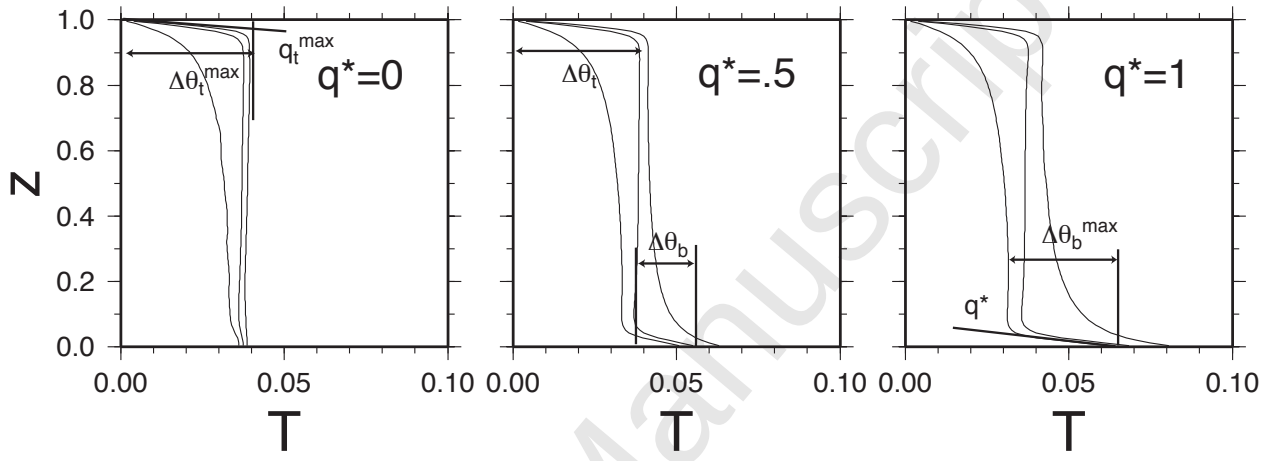

Fig. 2. Time-averaged temperatures as a function of depth. On each panel, three profiles are displayed: horizontally-averaged , minimum and maximum temperatures at a given depth. Three values of the fraction of basal heating (q^*) are shown for free-slip boundaries and $\mathrm{Ra}_f = 10^8$. Bold lines and arrows describe the procedure chosen to evaluate the temperature differences ($\Delta\theta_t, \Delta\theta_b$) and the maximum (minimum) temperature differences ($\Delta\theta_t^{max}, \Delta\theta_b^{max}$) from the various profiles. Note that since heat-flux is prescribed on the bottom boundary, all profiles have the same slope there while the slopes differ at the the top boundary ($q_t^{max} > 1$).

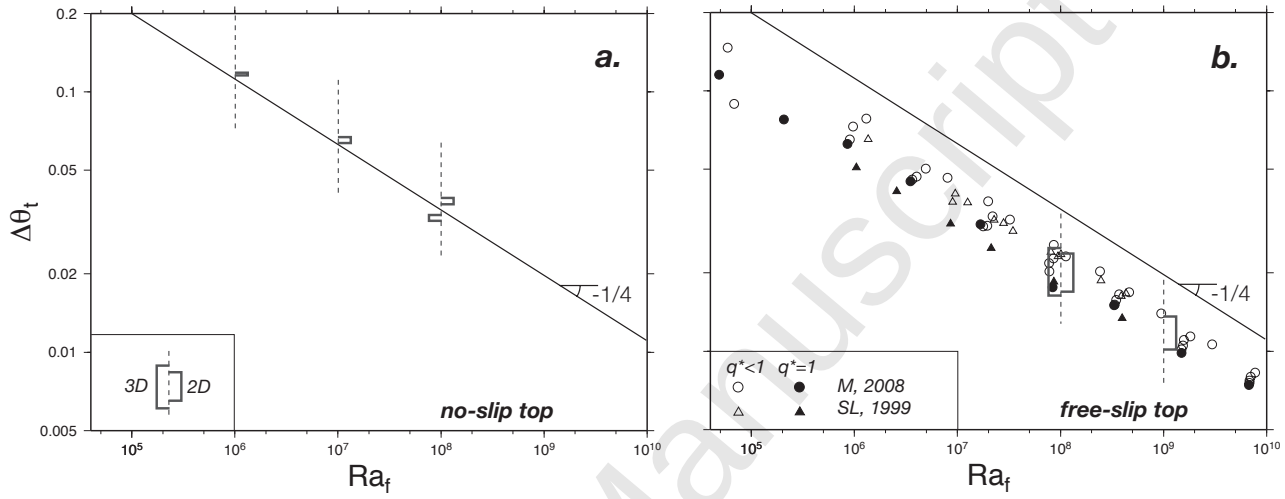

Fig. 3. Temperature difference across top thermal boundary layer ($\Delta\theta_t$) as a function of the flux-based Rayleigh number (Ra_f). The straight line shows an ideal $\mathrm{Ra}_f^{-1/4}$ scaling as in Eq. 1. (a) Results from numerical experiments with a no-slip top boundary. For each of the three values of Ra_f, the ranges including all the result is displayed as a rectangle with a missing side (on the right for 3D, on the left for 2D). (b) Results from numerical experiments with a free-slip top boundary. As in (a) results from this study are displayed using rectangles. Results from previous studies are shown by circles (Moore, 2008) and triangles (Sotin and Labrosse, 1999). Empty symbols refer to mixed heating while filled symbols refer to only heating from below.

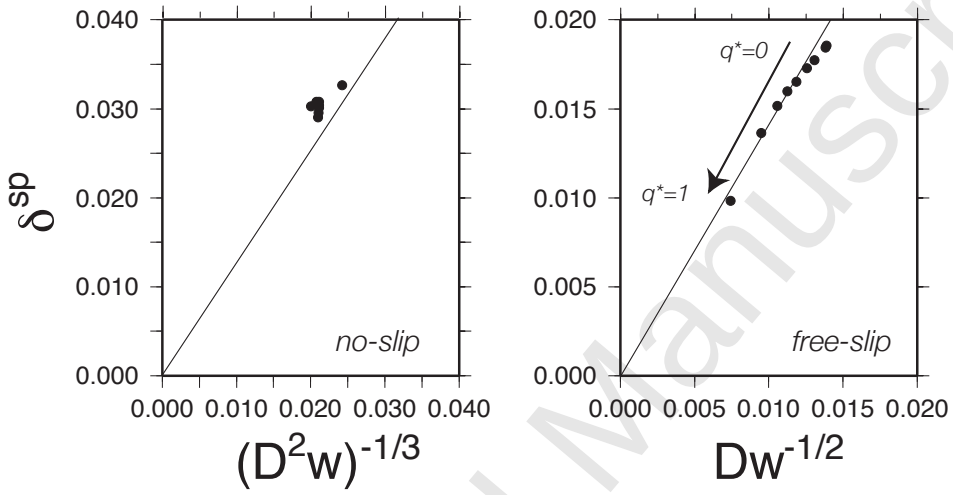

Fig. 4. Stagnation-point boundary layer thickness $\delta^{sp}(= \Delta\theta_t^{max}/q_t^{max})$ as a function of the appropriate vertical velocity derivative $D^n W$ (computed from the maximum vertical velocity profile at each time-step, averaged through time). Purely no-slip and purely free-slip results also shown in Figure 1-a,b ($\mathrm{Ra}_f = 10^8$). Lines refer to the simple stagnation-point scaling indicated in the text (3).